



# Negative Index Materials Using Atomic Transitions: Progress and Challenges

Deniz D. Yavuz<sup>1</sup>, Zachary N. Buckholtz

Department of Physics, University of Wisconsin, Madison, WI, United States

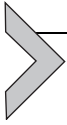
<sup>1</sup>Corresponding author: e-mail address: yavuz@wisc.edu

## Contents

1. Introduction	430
1.1 Why Study Negative Refraction Using Atomic Transitions	432
2. Negative Refraction Using Atomic Transitions	435
3. Experimental Implementation in Rare-Earth-Doped Solids	439
4. Magnetic Response in a Europium-Doped Crystal	443
4.1 Rabi Flopping	447
4.2 Verification of the Magnetic Dipole Nature of the Transition	451
5. Left-Handed Waves: EIPM Scheme	454
5.1 Proposed Scheme for Left-Handed Waves in Eu:YSO	455
5.2 Refraction at an Interface	457
6. Conclusions	459
Acknowledgments	460
References	460
Further Reading	464

## Abstract

Optics and optical tools are central to many research areas of physical sciences and engineering. Over the last 2 decades, there has been a growing interest in a new generation of optical tools using materials that are not available in nature. These materials, called negative index materials, offer the promise of devices with unique capabilities; for example, super resolution lenses and optical cloaks. All constructed negative index materials have so far utilized artificial structures such as patterns of metal wires and loops to produce the desired optical property. In this chapter, we will review an alternative and in many ways complementary approach to constructing negative index materials. Instead of relying on engineered patterns, the idea is to utilize the resonances provided to us by nature, i.e., naturally occurring transitions of atoms or ions. We discuss (i) the schemes for negative index using atomic transitions, (ii) recent experiments where resonant magnetic response in a europium-doped crystal was observed, and (iii) future prospects and challenges for constructing negative index materials using atomic transitions.



## 1. INTRODUCTION

Optics and optical tools have played a key role in the development of the physical sciences and engineering over the last century. In particular, after the invention of the laser in 1960, optical tools have penetrated into and revolutionized many fields of science including biological imaging and nanotechnology. Over the last 2 decades, a new generation of optical tools has been proposed and continually investigated, using materials that are not available in nature (Houck et al., 2003; Lezec et al., 2007; Pendry, 2000; Pendry et al., 2012; Shelby et al., 2001; Smith and Kroll, 2000; Veselago, 1968). In the future, these materials, called negative index materials (also commonly referred to as metamaterials), may allow the construction of optical devices with unique capabilities. For example, it has been proposed that negative index lenses can, in principle, image objects with a resolution much better than the wavelength of the imaging light (so-called “perfect lenses”) (Cubukcu et al., 2003; Fang et al., 2005; Pendry, 2000; Smolyaninov et al., 2007). Negative index materials can also be designed to eliminate scattering in certain regions of the electromagnetic spectrum with possible cloaking applications (Ergin et al., 2010; Schurig et al., 2006; Valentine et al., 2009; Xianzhong et al., 2011). The unique capabilities of negative index materials result from their unusual optical properties. In these materials, the propagating electromagnetic waves are left handed; i.e., electric field, magnetic field, and the  $k$ -vector form a left-handed triad instead of the usual right-hand rule. For these waves, the Poynting and the  $k$  vectors are antiparallel (as opposed to parallel), the Doppler effect is reversed (if a source is moving toward a detector, the frequency of the emitted waves is reduced), and there is radiation attraction (instead of radiation pressure). Because of these highly unusual optical properties and possible important practical applications, negative index research has attracted an increasingly growing attention over the last 2 decades. Today there are hundreds of research groups around the world working in this exciting field exploring either practical or more fundamental aspects of negative index materials.

It is now well understood that negative index materials rely critically on their ability to interact strongly with both the electric and the magnetic fields of light; i.e., both the permittivity and permeability of the material must be substantially different from their values in free space (Veselago, 1968). This is usually quite difficult to achieve, especially in the optical region of the spectrum since materials generally do not respond to the magnetic field of light at

such high frequencies. These difficulties can be overcome and since the initial pioneering experiments (Shelby et al., 2001), the type, and the variety of constructed negative index metamaterials have grown substantially. (The term metamaterials is currently used for a wide range of artificial optical devices. Throughout this review, we will focus on specifically negative index metamaterials.) These materials are now routinely constructed in the microwave, terahertz, or the optical domain, can be surface based or bulk in three dimensions, and can be engineered using a variety of nanolithography techniques (Chen et al., 2016; Ferraria et al., 2015; Lapine et al., 2014). Although they differ greatly in their details, up until now, all constructed negative index materials have utilized artificial structures such as patterns of metal wires and loops to produce the desired optical property. The sizes of these wires and loops are chosen to provide resonant interaction with electromagnetic waves in a certain region of the spectrum. Negative index metamaterials traditionally utilized all metal or metal/dielectric structures with very large absorptive ohmic losses and heat dissipation. One approach for overcoming absorption is to use active metamaterials, which incorporate gain in their design (Boardman et al., 2011; Hess et al., 2012; High et al., 2015; Xiao et al., 2010). Another approach is to use surface-based devices, called metasurfaces, in which the waves are confined to the surface resulting in reduced losses (Chen et al., 2016; Glybovski et al., 2016). However, metasurfaces are better suited for more traditional optical functionalities so many of the exciting applications of negative index such as perfect lenses cannot be implemented. Over the last 5 years, there has also been important progress in constructing all-dielectric metamaterials utilizing Mie resonances in high-refractive index nanoresonators (Jahani and Jacob, 2016; Moitra et al., 2013; Zhao et al., 2009). All-dielectric metamaterials are transparent and have demonstrated a number of important functionalities such as magnetic mirrors and zero-index devices. These functionalities have also been restricted to surfaces, and it has not yet been possible to achieve a negative refractive index in a three-dimensional device using an all-dielectric approach. Although it has been 16 years since the first experimental demonstration of negative refraction, negative index materials with good optical quality that can be integrated into a real-life device have not yet been constructed. This motivates exploring different approaches to achieving negative index, and this is precisely the subject of this review chapter.

The goal of this chapter is to discuss an alternative and in many ways complementary approach to constructing negative index materials. Here, instead of relying on engineered patterns, the idea is to use sharp transitions

of atoms and ions: i.e., to utilize the resonances provided to us by nature. The possibility of constructing negative index materials using sharp transitions of atoms or ions was recognized early on (Kastel et al., 2007, 2009; Oktel and Mustecaplioglu, 2004; Orth et al., 2013; Sikes and Yavuz, 2010, 2011; Thommen and Mandel, 2006). When an electron makes a transition from the ground level to an excited level, it can do so by either interacting with the electric field or the magnetic field of light. Depending on the nature of the interaction, these transitions are said to be electric dipole or magnetic dipole. The chief difficulty of using atomic transitions for negative index research is that in the optical region of the spectrum one essentially only encounters electric dipole transitions since they are stronger by about five orders of magnitude. It has become possible only very recently to interact strongly with the magnetic field of a laser beam and modify the permeability using resonant magnetic dipole transitions (Brewer et al., 2017). This experiment was performed using a rare-earth (europium)-doped crystal at cryogenic temperatures. Extending this experiment to higher doping concentrations and/or to stronger magnetic dipole transitions shows considerable promise for achieving negative index using atomic transitions in the near future. Furthermore, as we will discuss below, this experiment already has the required parameters for investigating many aspects of negative index-related phenomenon such as left-handed wave propagation and negative refraction at an interface using the recently suggested externally induced polarization and magnetization (EIPM) scheme. In this chapter, we will review (i) the schemes for negative index using atomic transitions, (ii) our recent experiments where we obtained resonant magnetic response in a europium-doped crystal, and (iii) future extensions of our experiments, and prospects and challenges for constructing negative index materials using atomic transitions.

## 1.1 Why Study Negative Refraction Using Atomic Transitions

The atomic approach has a fundamental advantage in the feature size and the uniformity of the constructed devices. In order to obtain good macroscopic response, metamaterials require the size of the engineered structures to be small compared to the wavelength of light. Owing to resolution limitations of lithographic techniques, current metal-based metamaterials are limited to feature scales of about  $\lambda/5$  in the optical region of the spectrum (the quantity  $\lambda$  is the wavelength of light). In all-dielectric metamaterials, irrespective of the lithographic resolution, Mie resonances require spheres or cylinders of

specific sizes, which fundamentally sets the feature scale to a range of  $\lambda/2$  to  $\lambda/5$ . The feature size of metamaterials sets important limitations on the device performance: for example, the “perfect lenses” constructed using current metamaterials would be limited to a resolution of about  $\lambda/5$ . This is one of the main reasons why over the last 5 years the metamaterial research has shifted from negative index to metasurfaces and more traditional optical functionalities. In contrast, when atomic transitions are utilized, the unit-cell length of the crystal sets the scale for feature size since the individual emitters are atomic ions. The unit-cell lengths of typical crystals are at the level of 1 nm, which means that uniformity of order  $\lambda/1000$  in the optical region of the spectrum is, in principle, achievable at high doping concentrations. Even at low doping concentrations of order 0.1%, the spacing between radiating ions is about 10 unit-cell lengths, which results in uniformity of order  $\lambda/100$ .

The atomic approach is also uniquely equipped to combine negative index research with quantum optics, and therefore to possibly construct “quantum metamaterials.” We will discuss two possible future experiments that show the power of this approach. (i) Rare-earth-doped crystals at cryogenic temperatures have narrow optical and hyperfine linewidths, and many quantum interference effects can be observed in these systems. For example, using electromagnetically induced transparency (EIT) and related techniques (Harris, 1997; Scully and Zubairy, 1997), single-photon probe laser pulses can be slowed down and stopped inside the crystal, and their quantum state can be mapped onto a “spin-wave” of the hyperfine transition. If the crystal can be induced to have a negative refractive index at the probe frequency, this opens up the possibility of constructing quantum storage devices with highly unusual optical properties. For example, we will be able to investigate storage and retrieval of quantum states of left-handed photons. Another possibility is to store photons whose spatial structure may be much smaller compared to the wavelength of light. This may allow constructing quantum memories whose spatial resolution is not limited by the wavelength of light. (ii) In these systems, it is relatively straightforward to address a single ion in the crystal (Kolesov et al., 2012). As shown in Fig. 1, by using a tightly focused beam and using the frequency selectivity of a narrow spectral hole under the inhomogeneous profile, a single rare-earth ion can be excited near the focal spot. This single ion can then be used as a single-photon emission source. If a section of the crystal is designed to be a “perfect-lens,” such a single-photon source can then be imaged to a plane with subwavelength resolution. This opens up the possibility of constructing single-photon sources with nanoscale pointing/addressing resolution.

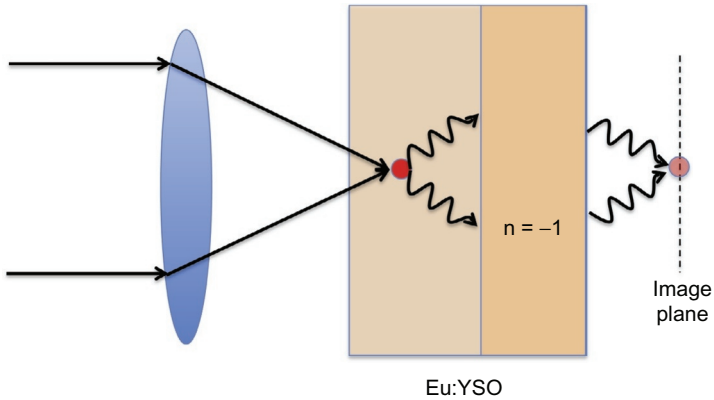
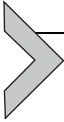


**Fig. 1** A single-photon emitter with nanoscale pointing resolution. Using frequency selectivity of spectral hole burning techniques, a focused laser beam can be used to excite a single ion in the ensemble. This single ion can then be used as a single-photon emitter, which can be imaged with nanoscale resolution if a section of the crystal has a refractive index of  $n = -1$ .

There are also practical reasons for studying atomic transitions for metamaterial research. As we will discuss later, our experiments are conducted in high-quality dielectric crystals doped with rare-earth ions. Therefore, these systems do not suffer from intrinsic optical losses associated with metals, as well as the low optical quality of many of the engineered structures. Also, in the atomic approach, in the spirit of EIT, the optical response is controlled by intense control laser beams. As a result, the optical properties of the constructed materials can be dynamically modified in real time by modulating the intensity or the frequency of the control lasers.

Despite these advantages, it is also important to note that there are drawbacks of using atomic transitions for negative index research. The first important drawback is that we are largely limited to wavelengths that are provided to us by nature. Also our current experimental system operates at cryogenic temperatures, which is a significant complication for device applications. Although there are prospects for extending these experiments to room temperature, there are also open questions that need to be addressed in this regard. Finally narrow linewidths of atomic transitions necessarily translate into inherently narrowband metamaterials. Traditional structured metamaterials typically operate over a few to tens of nanometer wavelength range. In contrast, there are two frequency scales in atomic systems that set the bandwidth: the inhomogeneous linewidths of doped crystals at cryogenic temperatures (which is of order a few GHz) and the Rabi frequency

of the control lasers (which is typically of order a few MHz). While these frequency scales are much narrower compared to the bandwidths of current metamaterials, as mentioned earlier, there are also inherent advantages in using narrow transitions. Atomic transitions may allow, for the first time, to truly combine metamaterial research with quantum optics.



## 2. NEGATIVE REFRACTION USING ATOMIC TRANSITIONS

Veselago's original proposal for achieving a negative index of refraction requires simultaneously negative permittivity and permeability of the material (Veselago, 1968). Using this idea, Oktel and Mustecaplioglu (2004) and Thommen and Mandel (2006) were the first to study the possibility of negative refraction in driven atomic systems. As mentioned earlier, the chief difficulty of this approach in the optical region of the spectrum is the weakness of the magnetic response. Since typical transition magnetic dipole moments are much smaller than electric dipole moments, achieving negative permeability requires impractically large atomic densities. A key progress on this problem was made when it was recognized that using chirality (magnetolectric cross coupling), the requirement on atomic densities can be relaxed by more than two orders of magnitude (Kastel et al., 2007, 2009). This is because, magnetolectric cross-coupling coefficients are smaller by only a factor of  $\alpha$  (fine structure constant) compared to the electric susceptibility (as opposed to the magnetic susceptibility being smaller by a factor of  $\alpha^2$ ). As a result, it becomes possible to obtain a negative refractive index without requiring a negative permeability. Instead, a magnetic susceptibility of about  $\chi_M \approx 10^{-2}$  is sufficient to obtain a negative refractive index. Building on this idea, Kastel et al. (2007, 2009) suggested a promising scheme that achieves negative refraction with low absorption using quantum interference. Their scheme utilizes the dark state of EIT to reduce absorption while enhancing chiral response. In a related idea, we suggested a scheme that relies on chirality and Raman transitions to achieve a negative refractive index (Sikes and Yavuz, 2010, 2011). One key advantage of this scheme is that by using the interference of two Raman transitions (one amplifying and one absorptive in nature), one can obtain a negative refractive index with negligible absorption. Fig. 2 shows a numerical calculation for a model atomic system with densities of  $2 \times 10^{16}$  atoms/cm<sup>3</sup> (left) and  $5 \times 10^{16}$  atoms/cm<sup>3</sup> (right). Here, we consider "ultracold" atomic system by taking the optical transition linewidths to be 1 MHz, which is a highly stringent requirement. As we will discuss below, such a system can, for

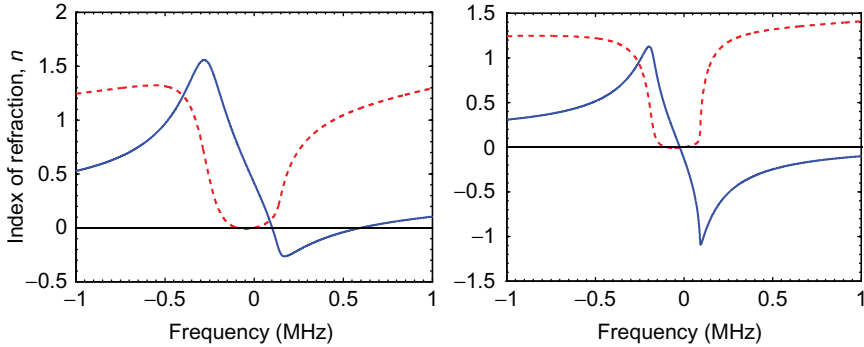


**Fig. 2** The real (solid blue line) and the imaginary (dashed red line) parts of the index of refraction for an atomic density of  $2 \times 10^{16}/\text{cm}^3$  (left) and  $5 \times 10^{16}/\text{cm}^3$  (right) in a model atomic system. From Sikes, D.E., Yavuz, D.D., 2010. Negative refraction with low absorption using Raman transitions with magneto-electric coupling. *Phys. Rev. A* 82, 011806.

example, be prepared using rare-earth-doped crystals at cryogenic temperatures and spectral hole burning techniques. The plots show the real and imaginary parts of the refractive index as the detuning from one of the Raman transitions is varied. The plots demonstrate that near a slightly positive frequency detuning of about 0.1 MHz, one can obtain a negative refractive index with low absorption using this scheme.

The energy level structure of our Raman-based negative index scheme is shown in Fig. 3. We wish to achieve a negative index of refraction for the probe laser beam with electric and magnetic field components of  $E_p$  and  $B_p$ , respectively. We take the atomic system to have a strong magnetic transition with dipole moment  $\mu_{gm}$  near the frequency of the probe laser beam. It is important to note that the system does not have a strong electric dipole transition at exactly the probe laser frequency, which gives substantial flexibility to the energy level structure. The electric dipole response is obtained by using two-photon Raman transitions through the excited state  $|e\rangle$ . Starting with the ground state  $|g\rangle$ , we induce two Raman transitions using the probe laser and two intense control lasers with electric field amplitudes  $E_{c1}$  and  $E_{c2}$ , respectively. Since the excitation configuration from the ground level is different ( $E_{c1}E_p^*$  vs  $E_pE_{c2}^*$ ), this scheme achieves two resonances: one amplifying and one absorptive in nature. The strength and the line center of these two resonances can be controlled by varying the intensities and the frequencies of the control lasers. It is the interference of these two resonances that allow for the control of the index of refraction while maintaining small absorption (Yavuz, 2005). The magnetoelectric cross coupling is achieved through coherent coupling of states  $|2\rangle$  and  $|m\rangle$  with

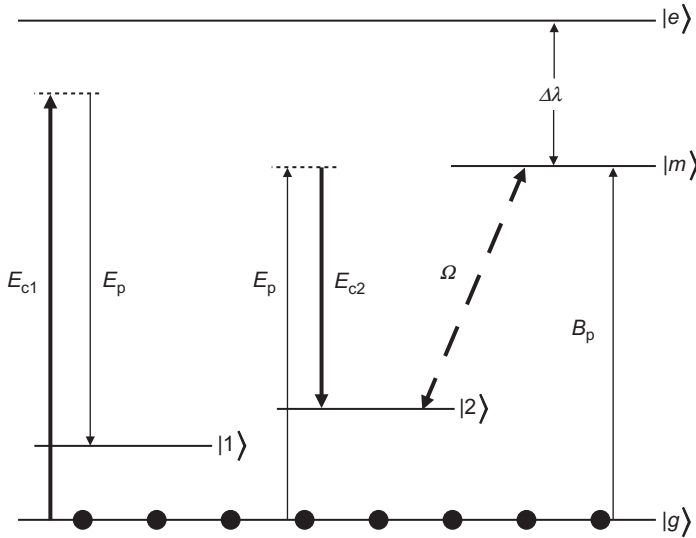


**Fig. 3** The energy level diagram of the proposed Raman-based negative index scheme.  $E_p$  and  $B_p$  are the electric field and magnetic field, respectively, components of the probe laser beam.  $|g\rangle \rightarrow |m\rangle$  is a magnetic dipole transition induced by the probe magnetic field  $B_p$ . Two strong control laser beams,  $E_{c1}$  and  $E_{c2}$ , induce two electric dipole Raman transitions for the probe beam. The Raman transitions can be far detuned from the excited state,  $|e\rangle$ . As a result, the system does not require  $|g\rangle \rightarrow |m\rangle$  and  $|g\rangle \rightarrow |e\rangle$  transitions to be at exactly the same wavelength.  $\Omega$  induces magnetolectric cross coupling (chirality). From Sikes, D.E., Yavuz, D.D., 2010. *Negative refraction with low absorption using Raman transitions with magneto-electric coupling*. *Phys. Rev. A* 82, 011806.

a separate laser beam of Rabi frequency  $\Omega$ . States  $|g\rangle$ ,  $|1\rangle$ ,  $|2\rangle$ , and  $|m\rangle$  have the same parity, which is the opposite of the parity of state  $|e\rangle$ . Since states  $|2\rangle$  and  $|m\rangle$  have the same parity, the coherent coupling  $\Omega$  cannot be electric dipole, but instead can be achieved through the magnetic field of a strong laser or through a separate two-photon transition (not shown). As we discuss below, states  $|g\rangle$ ,  $|1\rangle$ , and  $|2\rangle$  can be the hyperfine levels of the ground level. The quantity  $\Delta\lambda$  is the difference between the transition wavelengths of the electric dipole and magnetic dipole transitions.

One of the key advantages of the scheme of Fig. 3 is that it does not require electric and magnetic dipole transitions at exactly the same wavelength. The wavelength separation  $\Delta\lambda$  can be larger at the expense of an increase in the required control laser intensities. Fig. 4 demonstrates this result. Here we plot the control laser intensity that is required to obtain results comparable to that of Fig. 2 as the wavelength separation between the transitions,  $\Delta\lambda$ , is varied. The transition wavelengths may be different

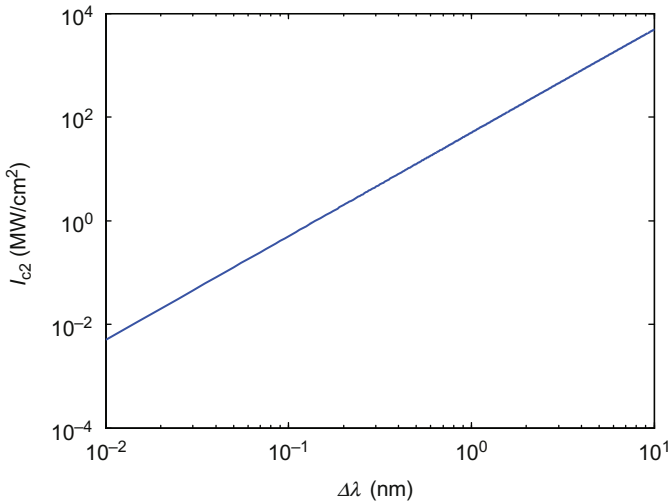
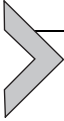


**Fig. 4** The control laser intensity that is required to obtain results comparable to those of Fig. 2 as a function of the wavelength separation between the transitions.  $I_{c1}$  shows a similar trend (not shown). From Sikes, D.E., Yavuz, D.D., 2010. *Negative refraction with low absorption using Raman transitions with magneto-electric coupling*. *Phys. Rev. A* 82, 011806.

by more than  $\Delta\lambda = 10$  nm, and the scheme will still work with experimentally accessible laser systems. This gives considerable flexibility in the energy level structure. The fact that the probe laser is detuned from the strong electric dipole transition by an amount  $\Delta\lambda$  also helps controlling various second-order effects such as reabsorption of spontaneously emitted photons (radiation trapping) (Fleischhauer, 1999).

The results that are summarized in this section clarify the experimental requirements that need to be met for observing a negative refractive index using atomic transitions: (i) the first requirement is an atomic or an ionic ensemble (or a mixture of two ensembles) that has a strong magnetic dipole and an electric dipole transition with transition wavelengths within at most about 10 nm of each other. These transitions should have magnetic dipole and electric dipole transition matrix elements of about one atomic unit. (ii) Atomic or ionic densities at or higher than  $10^{16}/\text{cm}^3$  with optical transition linewidths 1 MHz or narrower (i.e., ultracold) are necessary. (iii) There should be a sufficient number of stable ground levels (such as hyperfine levels) to allow for narrow Raman transitions or EIT to be implemented. While these are quite challenging experimental requirements, as we discuss below, rare-earth-doped crystals at cryogenic temperatures show considerable promise for meeting these requirements.



### 3. EXPERIMENTAL IMPLEMENTATION IN RARE-EARTH-DOPED SOLIDS

Rare earths of the lanthanide series have one of the most complex electronic spectra of known elements due to the rich structure of the open  $f$ -shell. Although the first spectra of rare earths were obtained as early as the 1930s, detailed investigation and understanding of their electronic structure had to wait until the 1960s when tunable laser sources were developed and computers became powerful enough to enable reasonably accurate calculations (Dieke and Crosswhite, 1963; Macfarlane, 2002; Taylor and Darby, 1972; Wybourne, 1965). The interest in rare earths has been continually growing over the last 2 decades due to applications in diverse research areas including quantum information storage and precision measurement of the electron electric dipole moment.

We note that a number of neutral rare-earth species have been laser cooled and trapped (Berglund et al., 2008; Lu et al., 2010; McClelland and Hanssen, 2006; Takasu et al., 2003). Of particular importance, quantum degenerate gases of ultracold erbium, dysprosium, and ytterbium have been demonstrated (Aikawa et al., 2012; Fukuhara et al., 2007; Lu et al., 2012). Although these are exciting developments, neutral ultracold clouds currently do not have the necessary densities for achieving negative refractive index. The highest demonstrated density in these systems is about  $10^{14}/\text{cm}^3$ , which is at least two orders of magnitude smaller than the densities required for negative index. Furthermore, ultracold gas clouds will pose many challenges for possible future device-type applications.

Rare-earth ionic ensembles in doped crystals at cryogenic temperatures offer a more promising route for negative index. We first would like to summarize a number of defining features of these systems (Macfarlane, 2002).

(i) Rare earths typically form trivalent ions in crystals with only  $4f$  electrons remaining in the outer shell in the ground configuration. The  $4f$ -shell is tightly bound to the nucleus and the  $4f$  electronic configuration interacts weakly with the crystal environment. As a result, the intraconfigurational  $4f \rightarrow 4f$  transitions are sharp, and they are very much like free-ion transitions that are only weakly perturbed by the crystal field. At cryogenic temperatures, homogeneous linewidths well below 1 MHz are routinely observed for the  $4f \rightarrow 4f$  transitions. Optically excited fluorescence level lifetimes exceeding 1 ms have also been demonstrated in these systems (Equall et al., 1994; Macfarlane and Shelby, 1987). Furthermore, due to the absence

of atomic motion, there is no Doppler broadening nor atomic diffusion. Because of these properties, rare-earth-doped crystals closely resemble ultracold clouds.

(ii) Owing to the richness of the electronic structure of the  $4f$ -shell, magnetic dipole transitions in the optical region can be found within the intraconfigurational  $4f \rightarrow 4f$  transitions. In a free ion, intraconfigurational  $4f \rightarrow 4f$  transitions are electric dipole forbidden since both lower and upper states belong to the same electronic configuration and have the same parity. In a crystal, some of the transitions become weakly electric dipole allowed due to mixing with the crystal field, so-called forced electric dipole transitions. Furthermore, hyperfine levels of the ground level are stable and long-lived, and they can be used to induce Raman transitions for the probe laser beam.

(iii) These systems routinely use doping fractions exceeding 0.1%, which corresponds to rare-earth ion densities exceeding  $10^{19}/\text{cm}^3$ . These densities are much higher than what can be achieved in neutral ultracold clouds or atomic vapors. The rare-earth ion-ion interactions do not significantly effect the  $4f$  configuration at these densities.

(iv) Because of the weak interaction with the crystal field, there is an inhomogeneous broadening of the intraconfigurational  $4f \rightarrow 4f$  lines (Macfarlane, 2002). This broadening depends on the crystal host and the specific levels, but is typically a few GHz. This broadening is unusually small for a solid-state system, which is again a result of the  $4f$  configuration being relatively well shielded from the crystalline environment. Although a quantitative understanding of this broadening has not yet been developed, it is known to be a result of crystal strains and local variations in the crystal field.

Inhomogeneous broadening can be overcome at the expense of a reduction in effective atomic density using spectral hole burning techniques (Konz et al., 2003; Lauritzen et al., 2008; McAuslan et al., 2012). These techniques lie at the heart of the EIT and quantum memory demonstrations in these systems (Ham et al., 1997, 1999; Klein et al., 2007a, 2007b, 2008; Turukhin et al., 2001). The idea is to selectively optically pump a subset of the atoms whose resonance frequencies are within about 1 MHz of each other, using appropriate optical pumping lasers. One essentially burns a 1 MHz wide hole under the broad GHz inhomogeneous profile, and only uses atoms whose resonance frequencies lie within the hole. This reduces the usable atomic density to exceeding  $10^{19} \times (1 \text{ MHz}) / (1 \text{ GHz}) = 10^{16}/\text{cm}^3$ , which is still quite large compared to what can be achieved using other

approaches. One therefore obtains an “ultracold” ensemble with a density exceeding  $10^{16}/\text{cm}^3$ , with  $4f \rightarrow 4f$  intraconfigurational transition linewidths of about 1 MHz.

(v) Other electronic configurations such as  $4f5d$  extend significantly beyond the  $4f$ -shell, and strongly interact with the crystal field (Van Pieterse et al., 2002a, 2002b; Wegh and Meijerink, 1999). Free-ion levels are split through the crystal field and form a band of levels. Some of these levels may be lifetime broadened and the corresponding  $4f^x \rightarrow 4f^{x-1}5d$  interconfigurational transitions to these levels may have narrow linewidths. However, most levels of the  $4f5d$  configuration are strongly coupled to the crystal conduction band, and the corresponding excitations exhibit broad features.

For negative index in rare-earth-doped crystals, the magnetic response can be obtained using strong magnetic dipole intraconfigurational  $4f \rightarrow 4f$  transitions. Near such magnetic dipole transitions, the permeability of the crystal will be significantly modified. For modifying the permittivity, there are two options. One option would be to use forced electric dipole transitions again within the  $4f$ -shell. The other option would be to use detuned electric dipole excitation using the interconfigurational  $4f^x \rightarrow 4f^{x-1}5d$  transitions. For experimental implementation of these ideas, we have identified one promising candidate to be terbium-doped calcium fluoride ( $\text{Tb}^{+3}:\text{CaF}_2$ ).  $\text{Tb}^{+3}$  is the rare-earth ion with the smallest energy spacing between the  $4f$  and  $4f5d$  configurations (Dieke and Crosswhite, 1963; Ofelt, 1962; Peijzel et al., 2005). As a result, it is practical to obtain electric dipole response using detuned excitation from the ground level to the  $4f5d$  configuration.  $\text{CaF}_2$  host crystal has excellent mechanical and optical properties with good transmission through much of the optical region all the way down to 130 nm. The detailed energy level diagram is shown in Fig. 5. The ground level of  $\text{Tb}^{+3}$  is  $4f^8\ ^7F_6$  and has been established both experimentally and also through Hartree–Fock calculations (Carnall et al., 1968; Ofelt, 1962; Thomas et al., 1963). By using Cowan’s atomic structure code, we have identified a strong intraconfigurational  $4f^8\ ^7F_6 \rightarrow 4f^8\ ^5F_5$  magnetic dipole transition at a wavelength of 282 nm, with a transition strength of  $\langle J || \mu || J' \rangle = 0.2\mu_B$  (the quantity  $\mu_B$  is the Bohr magneton) (Cowan, 1981). Although this transition has not been observed experimentally, we have found two publications that calculate this transition wavelength to within a few nanometer of the predictions of the Cowan’s code (Carnall et al., 1968; Ofelt, 1962). The lowest level of the  $4f^75d$

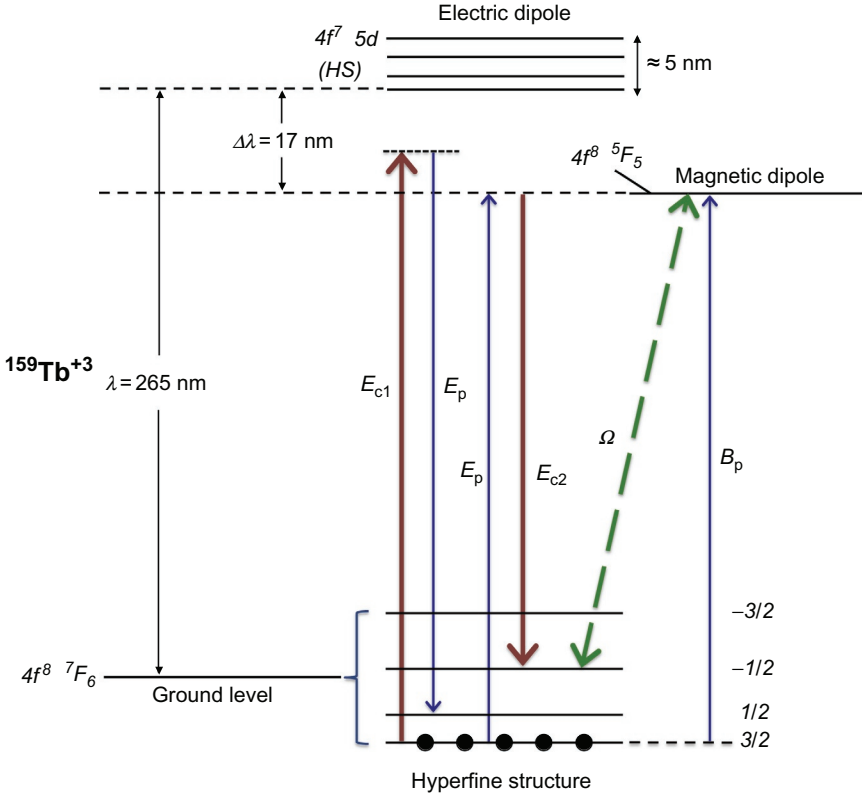
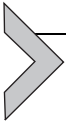


**Fig. 5** The proposed scheme for achieving negative refraction in  $^{159}\text{Tb}^{+3}$ . We have identified intraconfigurational  $4f^8 7F_6 \rightarrow 4f^8 5F_5$  transition at a wavelength of 284 nm as a strong magnetic dipole transition. The electric dipole response is obtained by Raman excitation through the  $4f^7 5d$  configuration. The laser beams are detuned by  $\Delta\lambda = 17 \text{ nm}$  from the bottom of the  $4f^7 5d$  configuration (the HS band). The hyperfine structure of the ground level in the presence of an external magnetic field is also shown.

configuration is so-called high-spin (HS) band, which has recently been observed experimentally in  $\text{Tb}^{+3}:\text{CaF}_2$  using synchrotron light from DESY (Van Pieterse et al., 2002b). In  $\text{CaF}_2$  crystal, this band starts at a wavelength of 265 nm with the levels split through the crystal field to a total width of about 5 nm. As shown in Fig. 5, the predicted wavelength difference between the magnetic dipole transition and the HS band is  $\Delta\lambda = 17 \text{ nm}$ .

The hyperfine structure of  $\text{Tb}^{+3}:\text{CaF}_2$  has been studied in detail in a number of publications (Liu et al., 1988; Pelletier-Allard and Pelletier, 1985). The crystal electric field lifts the degeneracy of the  $M_J$  levels and the ground level is a  $M_J = \pm 6$  doublet. The stable isotope of terbium is

$^{159}\text{Tb}$  with a nuclear spin of  $I = 3/2$ . Without any applied external magnetic field, the hyperfine interaction results in a pair of degenerate doublets,  $M_I = \pm 1/2$  and  $M_I = \pm 3/2$ . The degeneracy can be lifted through the Zeeman effect by applying an external DC magnetic field, producing the hyperfine structure shown in Fig. 5. The Zeeman shift of the levels is about 0.1 MHz/G, and as a result it is easy to achieve frequency splitting between the hyperfine levels of about 100 MHz. Owing to the relatively small spread in frequency, the probe, control, and magneto-optical cross-coupling lasers can be obtained from the same laser system using, for example, acousto-optic modulators (AOMs).



#### 4. MAGNETIC RESPONSE IN A EUROPIUM-DOPED CRYSTAL

When we first started thinking about possible initial experiments about 5 years ago, we encountered a big challenge. Although substantial magnetic dipole response had been observed from dielectrics with high-intensity ultrashort pulses (Oliviera and Rand, 2007; Rand et al., 2008), resonant magnetic response with near-monochromatic lasers using atomic transitions had never been observed in the optical region of the spectrum before. No experiment had ever shown that it is possible to interact strongly with the magnetic field of a laser beam and modify the permeability of the material substantially using atomic transitions. It immediately became clear to us this is what the first experiment should aim for. Without substantial magnetic response, it is not possible to be optimistic about future negative index experiments. In this section, we discuss our recent experiments where we demonstrated resonant magnetic response using the  $^7F_0 \rightarrow ^5D_1$  transition in europium ( $\text{Eu}^{+3}$ ) ions, and also observed strong field Rabi flopping of the ions using the magnetic field of the laser. We decided to focus on  $\text{Eu}^{+3}$  ions for the first experiments due to two key reasons: (i)  $\text{Eu}^{+3}$  has a half-filled  $f$ -shell ( $4f^6$ ) and has one of the richest  $f$ -shell structures of all the rare-earth ions. As a result, there are many strong magnetic dipole transitions in the optical region of the spectrum within the  $f$ -shell, with convenient transition wavelengths. (ii) There are only two rare-earth ions in which optical Raman schemes have been experimentally demonstrated. These are  $\text{Pr}^{+3}$  and  $\text{Eu}^{+3}$ . Of these two,  $\text{Pr}^{+3}$  is the more studied specie. However, the spacing between the ground hyperfine levels is about 100 MHz in  $\text{Eu}^{+3}$  vs about 10 MHz in  $\text{Pr}^{+3}$ . Larger hyperfine frequency spacing of  $\text{Eu}^{+3}$  is advantageous since it is easier to obtain the probe and coupling laser beams from

the same source in a straightforward way using AOMs. Larger hyperfine spacing also allows using shorter (larger bandwidth) pulses in the experiment.

The existence of magnetic dipole transitions in the optical region of the spectrum in rare-earth ions has been known for quite some time (Dieke and Crosswhite, 1963; Krupke, 1966; Macfarlane, 2002; Taylor and Darby, 1972; Weber and Schaufele, 1965; Wybourne, 1965). Early spectroscopic studies of rare-earth-doped crystals predicted the magnetic dipole nature of some of the transitions by studying the polarization properties of their fluorescence. The oscillator strengths of these transitions are lower by a factor of  $\alpha^2$  compared to electric dipole transitions. As a result, accessing these transitions is difficult since they are easily overwhelmed by nearby electric dipole transitions or are largely broadened by dissipative processes. Laser excitation of a magnetic dipole transition was achieved only 2 years ago in the pioneering work of Kasperczyk et al. (2015). They used europium-doped nanoparticles at room temperature and conclusively demonstrated the magnetic dipole nature of the  ${}^7F_0 \rightarrow {}^5D_1$  transition by utilizing a radially polarized focused laser. The only detailed spectroscopic study of the  ${}^7F_0 \rightarrow {}^5D_1$  transition before our experiments was performed by Shen and Kachru (1994) about 2 decades ago.

The  ${}^7F_0 \rightarrow {}^5D_1$  transition occurs in the green at a transition wavelength of 527.5 nm. To generate this color of light in our experiment, we frequency double high-power infrared light inside a cavity (Brewer et al., 2017). As shown in Fig. 6, the experiment starts with an infrared external cavity diode laser (ECDL) at a wavelength of 1055 nm. The ECDL has a free-running linewidth of about 0.5 MHz and an optical power of about 25 mW. We lock the ECDL to an ultralow expansion (ULE) glass cavity that serves as an absolute frequency reference for the experiment. Locking also narrows the ECDL laser linewidth to about 50 kHz. The ULE glass cavity is housed inside an ultrahigh vacuum chamber to reduce temperature fluctuations and mechanical perturbations.

The resonances of the ULE cavity have long-term frequency stability (over many days) better than 100 kHz. We use the Pound–Drever–Hall method to lock the frequency of the ECDL to one of the cavity resonances which is lined up with the peak of the inhomogeneous profile.

The ECDL output is amplified to an optical power exceeding 5 W using a commercial ytterbium-doped fiber amplifier. We frequency double the fiber amplifier output using cavity-based second harmonic generation with a 2-cm-long periodically poled KTP crystal (PPKTP). The poling period of

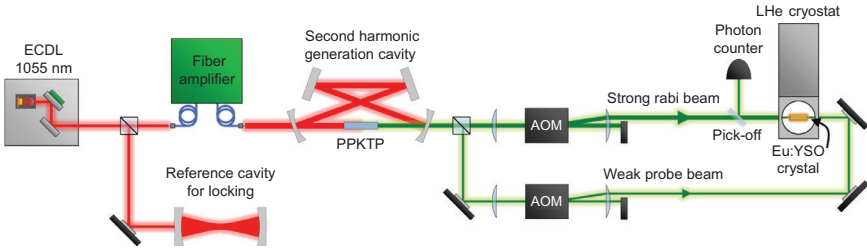


**Fig. 6** Simplified schematic of our experiments that was performed in a europium-doped crystal. The experiment starts with an infrared ECDL at a wavelength of 1055 nm. The ECDL is locked to a reference cavity, which is constructed from ULE glass. The ECDL seeds a ytterbium-doped fiber amplifier, which produces an optical power exceeding 5 W while maintaining the frequency stability of the ECDL. The fiber amplifier output is frequency doubled using cavity-based second harmonic generation with a periodically poled KTP (PPKTP) crystal. The output of the second harmonic generation cavity is split into two and acousto-optic modulators (AOM) are used to precisely control frequency and timing. The Eu:YSO crystal is housed in a continuous-flow liquid-helium cryostat. *From Brewer, N.R., Buckholtz, Z.N., Simmons, Z.J., Mueller, E.A., Yavuz, D.D., 2017. Coherent magnetic response at optical frequencies using atomic transitions. Phys. Rev. X 7, 011005.*

KTP is adjusted for phase matching at 1055 nm and is temperature controlled with a temperature stability at the level of 1 mK. One of the mirrors of the SHG cavity is mounted on a piezoelectric transducer, which is used to lock the amplifier output to the SHG. Using this set-up, we are able to produce green light at a wavelength of 527.5 nm with an optical power exceeding 1.5 W and an absolute frequency stability at the 100 kHz level. The green output from the doubling cavity is then split into two beams. Each beam goes through an AOM for frequency and timing control. We use a 3-mm-long europium-doped yttrium orthosilicate crystal ( $\text{Eu}^{+3}:\text{Y}_2\text{SiO}_5$ , hereafter abbreviated as Eu:YSO) which is housed in a continuous-flow liquid helium cryostat, and cooled to a temperature of 4.5 K. The crystal is cut such that light propagates along the  $b$  crystallographic axis, and the magnetic field of the laser is aligned with the  $D_1$  axis. Further details regarding our experimental system can be found in our recent publication (Brewer et al., 2017).

The  $4f$  configuration of  $\text{Eu}^{+3}$  is quite complex and extends over  $100,000 \text{ cm}^{-1}$  in energy. The lower levels of the  $4f$ -shell are shown in Fig. 7. Our crystal is doped at 0.1% with natural abundance europium (48%  $^{151}\text{Eu}$  and 52%  $^{153}\text{Eu}$ ), with both isotopes having a nuclear spin of  $I = 5/2$ . The hyperfine structure of the  $^{153}\text{Eu}$  isotope is also displayed in

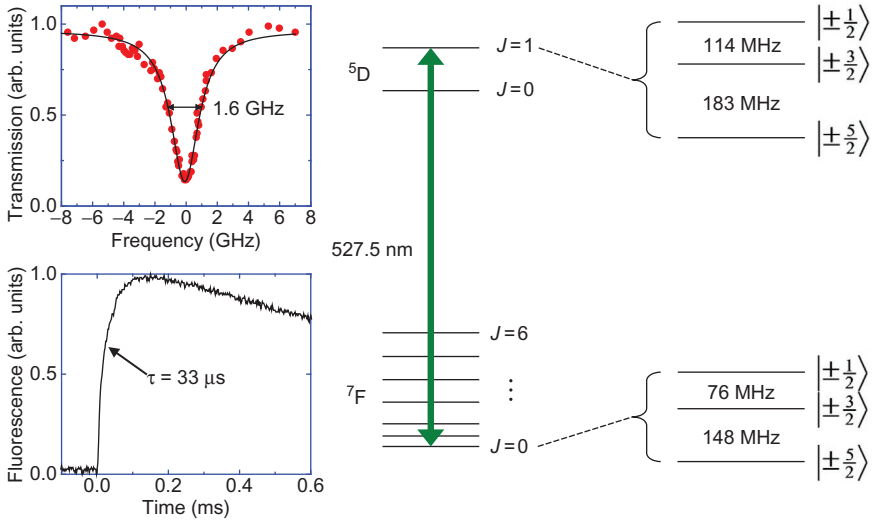


**Fig. 7** The levels of the  $4f$ -shell of  $\text{Eu}^{+3}$  ions with an energy below  $20,000 \text{ cm}^{-1}$ . We use the  $^7F_0 \rightarrow ^5D_1$  magnetic dipole transition at a wavelength of 527.5 nm. The hyperfine structure of the  $^{153}\text{Eu}^{+3}$  isotope with a nuclear spin of  $I = 5/2$  is also shown. The *numbers in the brackets* are the projection of the nuclear spin angular momentum,  $|\pm m_I\rangle$ . The *upper plot* shows the transmission of a weak probe laser beam as its frequency is scanned across the magnetic dipole transition. We observe an inhomogeneously broadened line (which is due to variations in the crystal field and crystal strains) with a width of 1.6 GHz, and a peak absorption of  $\exp(-1.8)$ . The *lower plot* shows the measurement of the homogeneous linewidth. Here, following excitation to the  $^5D_1$  level, we record the fluorescence from the  $^5D_0$  level to the ground  $F$  manifold. The initial sharp rise in the fluorescence is due to phonon-induced relaxation from  $^5D_1 \rightarrow ^5D_0$  which results in a homogeneous linewidth of  $\Gamma = 2\pi \times 4.8 \text{ kHz}$ . From Brewer, N.R., Buckholtz, Z.N., Simmons, Z.J., Mueller, E.A., Yavuz, D.D., 2017. Coherent magnetic response at optical frequencies using atomic transitions. *Phys. Rev. X* 7, 011005.

**Fig. 7** (the other isotope has a similar structure with smaller frequency separations between the hyperfine levels). The upper plot in **Fig. 7** is a measurement of the optical depth of the crystal. Here, we measure the transmission of a weak green probe laser beam as its frequency is scanned through the  $^7F_0 \rightarrow ^5D_1$  resonance. We observe an inhomogeneously broadened width of 1.6 GHz with an on-resonance optical depth of 1.8 through our crystal (i.e., the transmission at line center is  $e^{-1.8} = 0.17$ ). Because the inhomogeneous linewidth is large compared to the frequency spacing between the hyperfine levels, the hyperfine structure is not resolved in the transmission spectrum.

## 4.1 Rabi Flopping

The interaction strength between a resonant laser beam and the ionic ensemble is given by the corresponding Rabi frequency,  $\Omega = B\mu/h$ . Here,  $B$  is the magnetic field of the laser beam and  $\mu$  is the magnetic dipole matrix element. To be in the strong drive regime (Rabi flopping), the strength of the interaction must be large compared to the dissipative rates in the system. We therefore require  $\Omega \gg \Gamma$  where  $\Gamma$  is the homogeneous linewidth of the transition. In our system, the dominant contribution to  $\Gamma$  is phonon-induced relaxation of the excited level to its closest neighbor, the  ${}^5\text{D}_0$  level (the forced electric dipole  ${}^7\text{F}_0 \rightarrow {}^5\text{D}_0$  transition has recently been extensively utilized within the context of quantum memories (Konz et al., 2003; Lauritzen et al., 2012) due to its exceptionally narrow homogeneous linewidth). The lower plot in Fig. 7 shows the measurement of the relaxation time from the excited  ${}^5\text{D}_1$  level to its nearest neighbor  ${}^5\text{D}_0$  level. Here, we excite ions to the  ${}^5\text{D}_1$  level using a short green laser pulse. Immediately following this excitation, we record the fluorescence from the  ${}^5\text{D}_0$  level to the lower  $F$  manifold as a function of time. There is a sharp rise in the fluorescence followed by a slow decay. The initial sharp rise in the fluorescence is due to phonon-induced relaxation from  ${}^5\text{D}_1$  to  ${}^5\text{D}_0$ . The slow decay is a result of the radiative lifetime of the  ${}^5\text{D}_0$  level. The initial rise in the fluorescence has a time constant of  $\tau = 33 \mu\text{s}$ , which is also the non-radiative lifetime of the  ${}^5\text{D}_1$  level resulting in a homogeneous linewidth of  $\Gamma = 2\pi \times 4.8 \text{ kHz}$ . This is consistent with the spin-echo measurements of Shen and Kachru (1994). As we will discuss below, we can achieve Rabi frequencies approaching  $\Omega \approx 2\pi \times 1 \text{ MHz}$ , which is well within the strong drive regime  $\Omega \gg \Gamma$ .

Our Rabi flopping protocol is similar to those that have been implemented using electric dipole transitions. With the ions initialized to their ground level, we apply a Rabi flopping laser pulse of certain duration to the ions. The Rabi flopping laser pulse has an optical power of order 100 mW and is focused to a  $1/e^2$  intensity radius of  $56 \mu\text{m}$  in the crystal. The duration of the Rabi pulse is adjusted by switching the AOM on and off. After the Rabi beam is turned off, we turn on a  $5\text{-}\mu\text{s}$ -long probe pulse in a counterpropagating geometry and measure its transmission through the crystal. The probe power is attenuated to very low levels ( $<1 \text{ pW}$ ) so that the ionic populations are not significantly perturbed due to the presence of the probe. The probe power that is transmitted through the crystal is then measured with a commercial single-photon counting

module. We focus the probe laser beam to a spatial size substantially smaller than the Rabi laser ( $1/e^2$  intensity radius of about  $30\mu\text{m}$ ) so that the probe laser samples the peak of the Rabi laser spatial profile. Owing to the interaction with the Rabi flopping laser, the ionic population starts to flow coherently back and forth between the ground and excited levels. Depending on the duration of the Rabi pulse, the ions may be left in any one of the levels or in a superposition of the two at the end of the pulse. The Rabi flopping of the ions is then revealed by the transmission of the probe laser beam, through stimulated absorption and emission.

Fig. 8 shows one of our Rabi flopping measurements (data points) which is overlaid with numerical simulations (solid line). Here we measure the transmission of the probe laser through the crystal as the duration of the Rabi flopping laser pulse is varied. We observe a Rabi flopping cycle time of about  $1\mu\text{s}$ , which quickly dephases after about two cycles. As we will discuss below, the main contributions to the dephasing are the inhomogeneous broadening and the variation of the magnetic dipole matrix element between specific hyperfine transitions. For future negative index experiments, it is critical to know the value of the magnetic dipole matrix element since it directly determines how much the permeability can be modified. Because the Rabi cycle dephases quickly, there is a large uncertainty in the observed Rabi frequency (and hence in the inferred magnetic dipole matrix element) from a single flopping experiment. For accurate measurement of the magnetic dipole matrix element, we perform the Rabi flopping measurement of Fig. 8 at different Rabi laser pulse intensities. Fig. 9 shows the observed Rabi frequency as a function of laser intensity for 23 Rabi flopping measurements. The insets show six specific Rabi flopping experiments as the laser intensity is varied from  $5630$  to  $1510\text{ W/cm}^2$ . The solid line in the main plot is the expected square root fit to the observed data values. From this fit, we deduce the magnetic dipole matrix element to be  $\mu = (0.063 \pm 0.005)\mu_{\text{B}}$  for the magnetic field oriented along the quantization axis of the crystal (the  $D_1$  crystallographic axis). To the best of our knowledge, this is the first direct measurement of a magnetic dipole matrix element in the optical region of the spectrum.

Although highly complex, the wave functions of the  $4f$ -shell of  $\text{Eu}^{+3}$  have been reasonably well understood since the pioneering work of Ofelt (1962) many decades ago. Using intermediate-coupled wave functions and well-known methods of Racah algebra, calculations give a theoretical value of  $\mu = (0.096)\mu_{\text{B}}$  for the magnetic dipole matrix element (Wybourne and Smentek, 2007). The calculated theoretical value is therefore within 50%

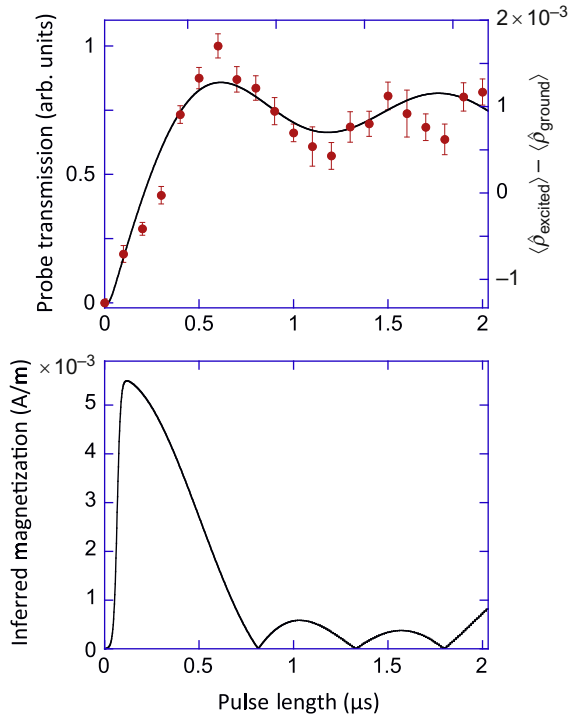


**Fig. 8** The transmission of the probe laser beam through the crystal as the duration of the Rabi pulse is varied. We observe a clear Rabi cycle with a frequency approaching 1 MHz. The Rabi oscillation quickly dephases due to a number of processes such as the variation of the magnetic dipole matrix element among various hyperfine transitions. The *solid line* is a numerical simulation that shows the calculated difference between the population of the excited hyperfine levels and the ground hyperfine levels,  $\langle \rho_{\text{excited}} \rangle - \langle \rho_{\text{ground}} \rangle$  as the width of the Rabi pulse is varied. In the numerical simulations, we solve the density matrix for a large number of atoms whose absolute transition frequencies are spread through the inhomogeneous profile, causing different hyperfine transitions to be resonant with the laser. The *lower plot* shows the inferred magnetization from the same simulations. See text for details. From Brewer, N.R., Buckholtz, Z.N., Simmons, Z.J., Mueller, E.A., Yavuz, D.D., 2017. Coherent magnetic response at optical frequencies using atomic transitions. *Phys. Rev. X* 7, 011005.

of the measured experimental value of the matrix element, and the reason for the discrepancy is currently not understood.

With the measured value of the magnetic dipole matrix element, we have performed density matrix simulations of the system. One of the main reasons for these simulations is to see if we can accurately reproduce the observed dephasing and the low contrast of the Rabi flopping curves. Another reason is to accurately predict the induced magnetization of the

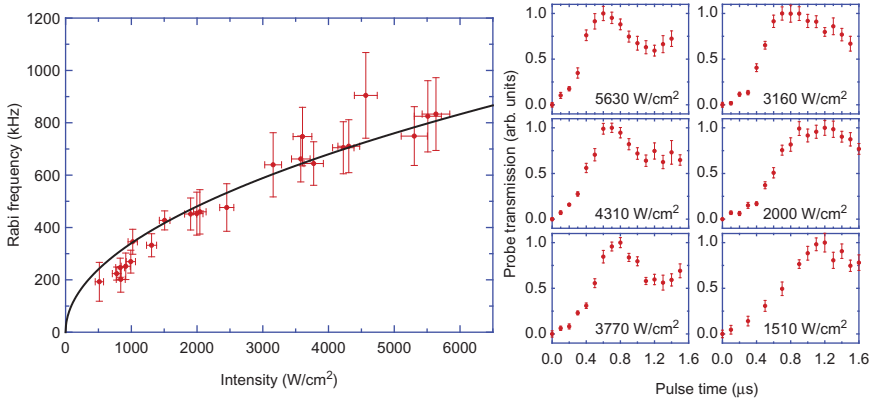


**Fig. 9** The observed Rabi flopping frequency as the laser intensity is varied for 23 different Rabi flopping experiments. From the square root fit to the data points (*the solid line*), we deduce a magnetic dipole matrix element of  $\mu = (0.063 \pm 0.005)\mu_B$ . The *insets* show six specific flopping experiments (probe transmission vs Rabi pulse duration) as the laser intensity is varied from 5630 to 1510 W/cm<sup>2</sup>. From Brewer, N.R., Buckholtz, Z.N., Simmons, Z.J., Mueller, E.A., Yavuz, D.D., 2017. Coherent magnetic response at optical frequencies using atomic transitions. *Phys. Rev. X* 7, 011005.

ensemble. In these numerical simulations, we take 80,000 ions with varying transition frequencies to model the inhomogeneous broadening of the ensemble. For each ion in the inhomogeneously broadened ensemble, we solve the time-dependent density matrix equations using the fourth-order Runge–Kutta algorithm. For the time domain evolution, we include all six hyperfine levels of the  ${}^7F_0 \rightarrow {}^5D_1$  transition as well as the  ${}^5D_0$  level; i.e., the size of the density matrix  $\rho$  is  $7 \times 7$ . We include both isotopes of europium in our calculations. The ions in the wings of the inhomogeneous distribution have a large detuning from the Rabi laser beam since this laser is tuned to the center of the profile. As a result, numerical integration of the ions in the wings requires a significantly smaller time step size, which substantially increases the run time of the simulation. To alleviate this problem, we focus on the center of the inhomogeneous profile and consider only the ions whose frequencies lie within 1 GHz of the line center. This is an excellent approximation since the ions in the wings contribute very little to the dynamics due to their large detuning from the laser. After numerical integration for each ion, we calculate the ensemble-averaged response by averaging the values of the density matrix elements at the end of numerical integration.

The solid line in Fig. 8 shows the calculated difference between the population of the excited hyperfine levels and the ground hyperfine levels,  $\langle \rho_{\text{excited}} \rangle - \langle \rho_{\text{ground}} \rangle$  as the width of the Rabi pulse is varied. Here, the

notation  $\langle \dots \rangle$  means that the quantities are averaged over the inhomogeneously broadened ensemble. There is good agreement between the numerical simulation and the experimental data points. Specifically, the contrast of the Rabi flopping cycle is well produced in the simulations. In the lower plot in Fig. 8, we calculate the inferred magnetization of the ensemble, by extracting the coherences (the off-diagonal density matrix elements) from the same numerical simulations,  $M = N \langle \rho_{\text{off-diagonal}} \rangle \mu$  (the quantity  $N$  is the ionic density). The simulations predict a peak value of  $M = 6.3 \times 10^{-3}$  A/m for the ensemble-averaged magnetization. Similar to the dephasing of the Rabi cycle, the induced magnetization also quickly dephases after reaching its peak value. This induced magnetization is similar in magnitude to magnetization produced in a loop with 1 mA current and loop area of  $1 \text{ cm}^2$ : very commonly produced in everyday circuits. However, the difference is that in our experiment the current oscillates at the optical frequency, at 570 THz.

These simulations verify that there are two main contributions to the observed dephasing of the Rabi flopping curves: (i) the Rabi flopping experiments are performed using the whole inhomogeneously broadened ensemble. As a result, the Rabi laser is only resonant with a small fraction of ions. The off-resonant ions flop at faster rates but with a reduced contrast. The observed signal is an ensemble average over all of these ions, which contributes to the dephasing of the Rabi cycle. (ii) There is a variation of the magnetic dipole matrix element between different hyperfine level transitions. Since we do not perform any optical pumping between hyperfine levels, Rabi flopping happens simultaneously between each ground and excited hyperfine level combination, i.e., there are nine different simultaneous excitations. The spread of the magnetic dipole matrix element between different excitations also contributes to the dephasing of the Rabi cycle.

## 4.2 Verification of the Magnetic Dipole Nature of the Transition

The magnetic dipole nature of the  ${}^7\text{F}_0 \rightarrow {}^5\text{D}_1$  transition was verified in Kasperczyk et al. (2015) using  $\text{Eu}^{+3}$  ions inside a different host crystal. We wanted to verify this measurement, so that we can be absolutely confident that the ions interacted with the magnetic field of the laser while they were experiencing Rabi flopping. To verify the magnetic dipole nature of the transition, Kasperczyk et al. (2015) utilized different spatial profiles of the magnetic field and the electric field of a tightly focused radially polarized laser. By using excitation of  $\text{Eu}^{+3}$ -doped nanoparticles, the spatial profile of the excitation field can be accurately mapped. We cannot use this method

since we use a millimeter-sized crystal in our experiment and cannot utilize the unique magnetic field profile of a tightly focused micron-scale radially polarized laser. To verify the magnetic dipole nature of the transition, we instead studied angle-dependent fluorescence from the crystal. For this purpose, we collect fluorescence in the orange from the  $^5D_0$  level to the lower  $F$  levels, with excitation green light propagating along each crystallographic axis and for two orthogonal polarizations ( $S$  and  $P$  polarized). The main idea is that because the crystal is highly anisotropic, as the crystal is rotated along a specific optical axis, for a specific polarization, either the angle between the magnetic field or the electric field of light with that axes changes. Consider  $S$  polarized light propagating along a certain axis of the crystal, as shown in part (a) of Fig. 10. The laser excites the crystal and we record the total fluorescence using a high-numerical aperture lens and a photodetector (not shown in Fig. 10). If the excitation is due to the interaction with the magnetic field, as the crystal is rotated along the axis shown, we would expect a change in the amount of excitation (and therefore the amount of fluorescence recorded). This is because, the crystal is highly anisotropic and as the crystal is rotated, the angle between the magnetic field and the optical axes would change. For this geometry, we would not expect variation in the

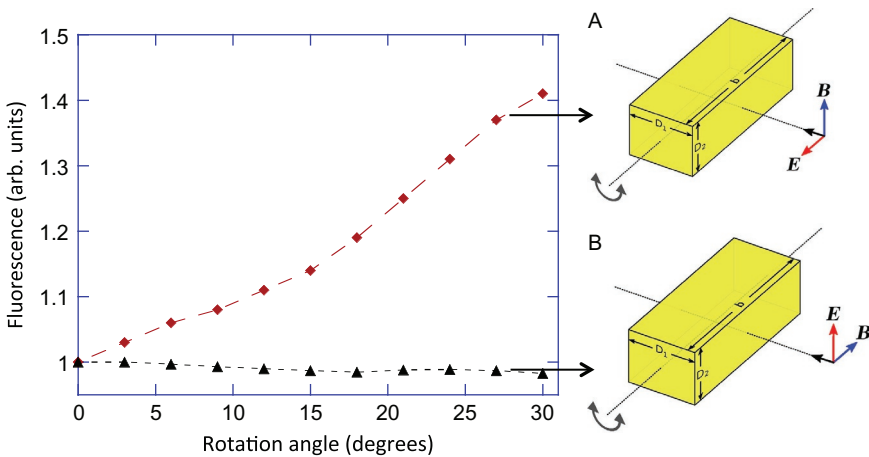


**Fig. 10** Fluorescence from the crystal as a function of the angle of incidence for  $S$  polarized [solid diamonds, schematic (a)], and  $P$  polarized [solid triangles, schematic (b)] light. The large increase in the fluorescence for  $S$  polarized light [schematic (a)] is due to a change of the direction of the angle of the magnetic field with the crystallographic axes. In contrast, when the angle of the electric field is varied [schematic (b)], there is negligible change in the fluorescence. From Brewer, N.R., Buckholtz, Z.N., Simmons, Z.J., Mueller, E.A., Yavuz, D.D., 2017. Coherent magnetic response at optical frequencies using atomic transitions. *Phys. Rev. X* 7, 011005.

fluorescence if the excitation is due to the electric field since its orientation with respect to all axes remains unchanged. For  $P$  polarized light [part (b) in Fig. 10], the roles of the electric and magnetic fields would be reversed. The plot in Fig. 10 shows this measurement for light propagating along the  $D_1$ -axis of the crystal with the crystal rotated around the  $b$ -axis. The measurement conclusively shows that the fluorescence changes when the direction of the  $B$ -field is varied and therefore proves the magnetic dipole nature of the excitation. We have repeated this measurement for light propagating along the other axes; the rest of the data can be found in our recent publication (Brewer et al., 2017). This measurement was performed using a thicker crystal with dimensions  $4\text{ mm} \times 5\text{ mm} \times 10\text{ mm}$  and outside the cryostat (i.e., at room temperature) so that we had access to all propagation axes of the crystal.

It is important to note that our experiment is not yet able to achieve a negative permeability (which is the most direct route to negative index), or modify the permeability substantially to obtain a negative index using the chiral scheme. From our magnetic dipole matrix element measurements, we can calculate the inferred magnetic susceptibility in our experiment. Fig. 11 shows

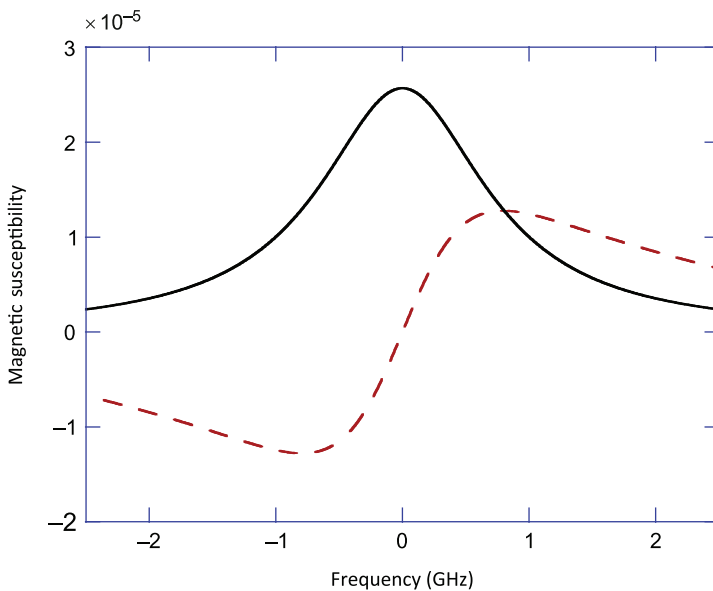
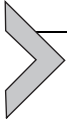


**Fig. 11** The inferred real (*dashed line*) and imaginary (*solid line*) parts of the magnetic susceptibility as the laser frequency is scanned across the  ${}^7F_0 \rightarrow {}^5D_1$  transition. From Brewer, N.R., Buckholtz, Z.N., Simmons, Z.J., Mueller, E.A., Yavuz, D.D., 2017. Coherent magnetic response at optical frequencies using atomic transitions. *Phys. Rev. X* 7, 011005.

the inferred real and imaginary parts of the magnetic susceptibility  $\chi_M$  as the probe laser is scanned through the  ${}^7F_0 \rightarrow {}^5D_1$  transition. From the magnetic susceptibility, the permeability of the material can be calculated using  $1 + \chi_M$ . Both real and imaginary parts of the susceptibility exceed  $10^{-5}$  near the resonance. As mentioned earlier, using chirality (magnetolectric cross coupling), even a magnetic susceptibility  $\chi_M \approx 10^{-2}$  is sufficient to induce a negative refractive index.



## 5. LEFT-HANDED WAVES: EIPM SCHEME

The earlier experiments have demonstrated for the first time that resonant magnetic response can be obtained using atomic transitions. One avenue for future research is to use stronger magnetic dipole transitions and/or higher-ionic densities, to increase the magnetic susceptibility to levels required to achieve negative index,  $\chi_M \approx 10^{-2}$ . Another approach would be to compensate for the inhomogeneous broadening using transition frequency-dependent AC Stark shifts. As discussed in [Yavuz et al. \(2013\)](#), Stark shifts can be adjusted to compensate for the transition frequency shifts, thereby reducing the inhomogeneous broadening. It also appears that if a material interacts with both the electric and magnetic field of light, then some physics of negative index materials can be explored immediately. In this section, we will discuss a specific scheme where the material is polarized and magnetized externally, i.e., using processes that do not depend on the probe laser beam ([Yavuz and Brewer, 2014](#)). We will refer to this scheme as EIPM. Compared to materials with a negative refractive index, there is one clear advantage of EIPM materials: the formation of left-handed waves does not require a specific threshold value for the value of the magnetic susceptibility. These materials appear to manifest much of the physics of negative index materials. As we will discuss below, the refraction angle from a “normal” right-handed material into an EIPM material is negative. However, there are also clear differences between EIPM and negative index materials. For example, the phase and group velocities of the left-handed waves are parallel (as opposed to antiparallel which is the case for negative index materials). Also, it is not yet clear if EIPM materials can be used for constructing lenses that beat the diffraction limit or for optical cloaks. The exact relationship between EIPM and negative index materials is currently an open problem.

A detailed description of the EIPM technique can be found in [Yavuz and Brewer \(2014\)](#). As shown in [Fig. 12](#), the key idea is to induce polarization  $P$  and magnetization  $M$  in the crystal of appropriate magnitude and phase

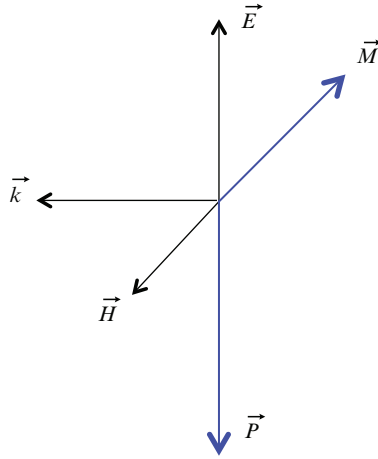


**Fig. 12** Left-handed waves inside a material with induced polarization and magnetization. If the medium is polarized and magnetized at the same frequency  $\omega$  with exactly the same  $k$ -vector, then there are forced wave solutions with the vectors  $E$ ,  $H$ , and  $k$  forming a left-handed triad. The solutions are such that the field quantities  $E$  and  $H$  are  $\pi$  out-of-phase with the induced polarization and magnetization. From Yavuz, D.D., Brewer, N.R., 2014. Left-handed electromagnetic waves in materials with induced polarization and magnetization. *Phys. Rev. A*, 90, 063807.

(using, for example, intense laser beams at different wavelengths and the nonlinear response which we discuss below). With the crystal externally polarized and magnetized, there are forced wave solutions with electric  $E$  and magnetic  $H$  fields along the axes shown in Fig. 12. The solutions are such that the fields are  $\pi$  out-of-phase with the induced polarization and magnetization, and  $E$ ,  $H$ , and  $k$  vectors form a left-handed triad (left-handed waves). We used numerical simulations of the full set of Maxwell's equations without any approximation to demonstrate the formation and stable propagation of these left-handed waves.

## 5.1 Proposed Scheme for Left-Handed Waves in Eu:YSO

Fig. 13 shows the specific scheme that we plan to pursue to excite left-handed waves. To generate the coherence of the  ${}^7F_0 \rightarrow {}^5D_1$  transition (and therefore induce magnetization), we plan to use two-photon excitation with an intense beam of infrared light at a wavelength of 1055 nm. The electric field of this laser beam is referred to as  $E_\omega$  in Fig. 13. As we discussed earlier, this laser is already available in our experiments since we frequency double this beam to produce the green light at 527.5 nm. With the crystal magnetized using the  $\text{Eu}^{+3}$  ions, one can then use the second-order

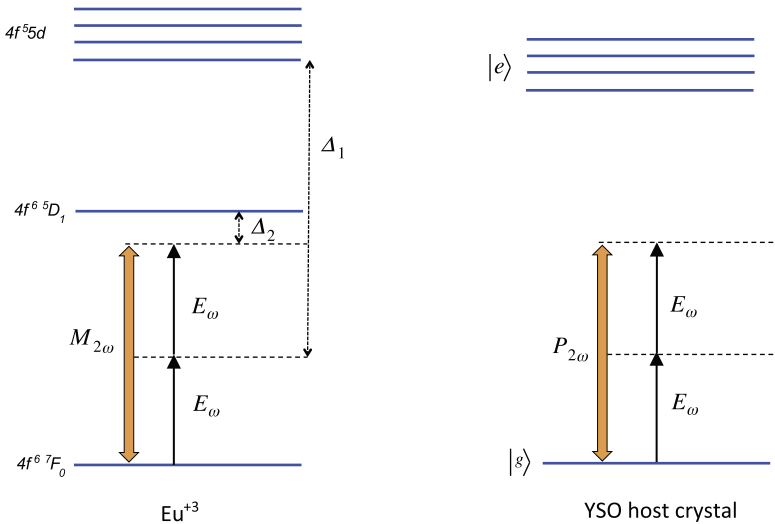


**Fig. 13** Proposed scheme for exciting left-handed waves in an Eu:YSO crystal. The magnetization is induced using the  ${}^7F_0 \rightarrow {}^5D_1$  strong magnetic dipole transition of the  $\text{Eu}^{+3}$  ions. Two-photon excitation with infrared light at a wavelength of 1055 nm (with field amplitude  $E_\omega$ ) is used to generate the coherence between the two levels. The two-photon excitation is through the  $4f5d$  configuration as the intermediate level. The polarization is induced using the second-order nonlinear response of the host crystal (YSO). The beam that induces the polarization is orthogonally polarized to the beam that induces magnetization.

nonlinear response of the host crystal to induce polarization. Owing to the second-order susceptibility,  $\chi^{(2)}$ , a separate infrared field  $E_\omega$  will produce a nonlinear polarization of magnitude  $P_{2\omega} = \chi^{(2)} E_\omega^2$ . The key advantage of the two-photon excitation scheme of Fig. 13 is that the lasers that induce the magnetization and polarization are at an infrared wavelength (1055 nm) whereas the left-handed waves in the crystal will be at the green wavelength (527.5 nm). As a result, it will be easy to filter out strong lasers that prepare the crystal and focus on the detection and measurements of the left-handed waves. A quick back of the envelope calculation immediately reveals that even if we assume a second-order susceptibility, which is many orders of magnitude smaller than common crystals [for example, quartz ( $\text{SiO}_2$ ) and many other crystals have  $\chi^{(2)} \approx 10^{-12}$  m/V], it is not difficult to induce a sufficiently large polarization in the crystal. If we then take the induced magnetization to be comparable to those achieved in the experiments described earlier, we calculate that one should be able to excite left-handed waves with optical powers at the level of 1  $\mu\text{W}$ . Although these are weak beams, they will be easily detectable using modern detection techniques such as electron multiplying CCD (EMCCD) cameras or single-photon counting modules.

A key issue will be how to demonstrate the left-handed nature of the produced waves. It may be possible to infer the left-handed nature of the waves while they are propagating inside the crystal. For example, with zero initial field condition (i.e., no green “seeding” beam), the established polarization and magnetization is expected to produce a pair of left-handed and right-handed waves propagating in opposite directions. The numerical simulations that discuss this effect in detail can be found in [Yavuz and Brewer \(2014\)](#). With a highly sensitive EMCCD, it will be possible to directly image the propagating waves since they will scatter photons from the inhomogeneities and impurities in the crystal. As the magnitudes of the induced polarization and magnetization is varied, the intensities of the counterpropagating left-handed and right-handed waves are predicted to follow a certain relationship. If such a relationship is observed in the experiment, it would be the first indication of the production of left-handed waves.

## 5.2 Refraction at an Interface

One of the most direct measurements of the left-handed waves would be to observe their refraction at an interface. As we discuss in this section, these waves should refract with a negative angle as they leave the crystal. Consider an electromagnetic wave refracting from a “normal,” right-handed material (medium 1) into an EIPM material (medium 2) as shown in [Fig. 14A](#). The refracted wave can be found using the well-known boundary conditions at the interface. Using an analysis which is very similar to Veselago’s original

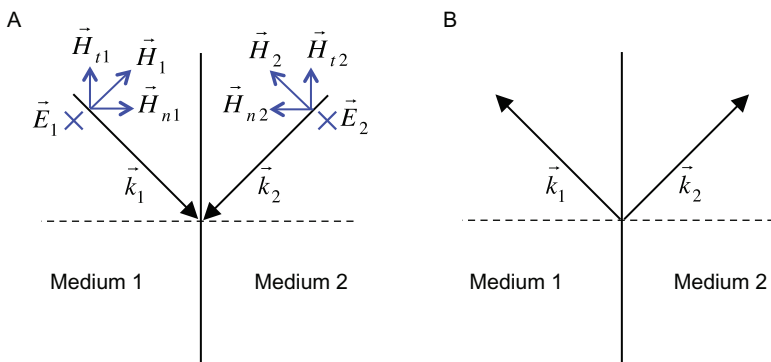


**Fig. 14** (A) Beam refraction from a “normal,” right-handed material into an EIPM material. Using the boundary conditions at the interface, the wave can be shown to refract with a negative angle. (B) The time-reversed case where the wave refracts from the EIPM material into the right-handed material. From Yavuz, D.D., Brewer, N.R., 2014. *Left-handed electromagnetic waves in materials with induced polarization and magnetization*. *Phys. Rev. A*, 90, 063807.

analysis of wave refraction into a negative index material (Veselago, 1968), it can be shown that the beam will refract at the interface with a negative angle with the  $k$  vectors as shown in Fig. 14A. Fig. 14B shows the time-reversed case where the wave refracts from the EIPM material into free space.

In Fig. 15, we numerically simulate the refraction of a wave from an EIPM material into free space (i.e., for the conditions of Fig. 14B). Here,

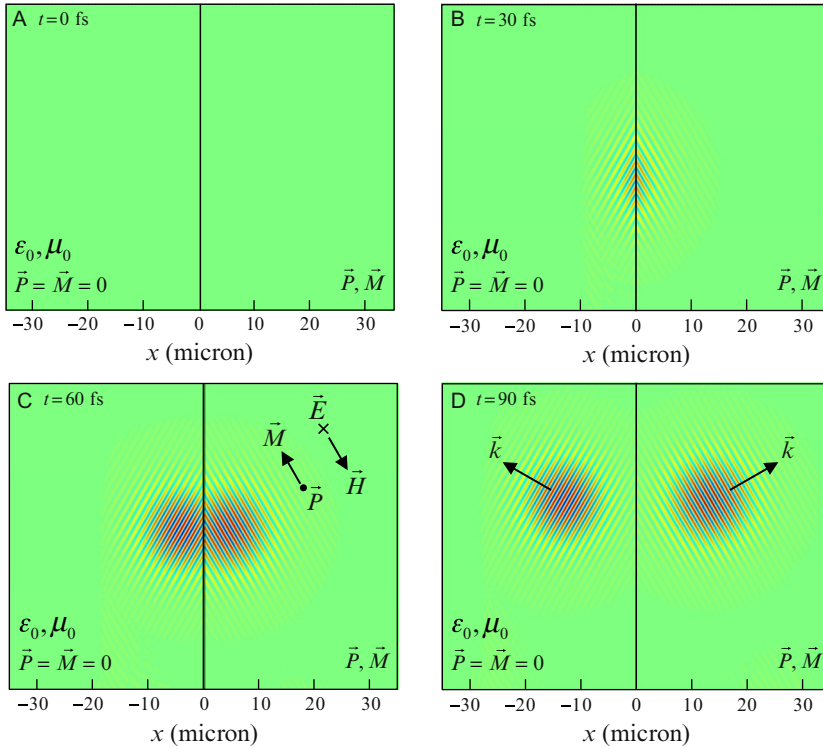


**Fig. 15** Wave refraction from an EIPM material into free space. Here, we assume polarization and magnetization waves in the material propagating along the  $k$ -vector as shown in Fig. 14B, and start with zero initial field values,  $H(x,y,t=0) = 0$  and  $E(x,y,t=0) = 0$  (i.e., there is no “seeding” pulse). (A) Before the polarization and magnetization exist in the region on the right, there is no generated EM wave. (B) Once the induced polarization and magnetization appear at the interface, a refracted right-handed wave appears in the region of free space. The polarization and magnetization generate the left-handed wave in the region of  $x > 0$ . (C) The direction of the polarization, magnetization, electric field, and magnetic field in the EIPM material are indicated. (D) After the pulse of polarization and magnetization has completely entered the region of  $x > 0$  the left-handed wave inside the material and the refracted right-handed wave outside the material propagate as expected. From Yavuz, D.D., Brewer, N.R., 2014. Left-handed electromagnetic waves in materials with induced polarization and magnetization. *Phys. Rev. A*, 90, 063807.

we assume polarization and magnetization wave packets in the material (prepared using the two-photon scheme of Fig. 13) propagating along the  $k$ -vector as shown in Fig. 14B, away from the interface. We start the numerical integration with zero initial field values,  $H(x,y,t=0)=0$  and  $E(x,y,t=0)=0$  (i.e., there is no “seeding” pulse), and solve Maxwell’s equations numerically using a finite difference method without any approximation. The induced polarization and magnetization generates the left-handed wave in the material, which in turn refracts into free space. The false-color plots in Fig. 15 show the snapshots for the electric field in the two spatial dimensions,  $x$  and  $y$ , at  $t=0$ ,  $t=30$  fs,  $t=60$  fs, and  $t=90$  fs, respectively. The boundary between the two regions is at  $x=0$ . The plots clearly show refraction into free space with a negative angle. If this is observed experimentally, it will be a clear indication of the left-handed nature of the propagating waves in the crystal.



## 6. CONCLUSIONS

Over the last 2 decades, there has been a resurgence of interest in studying near-resonant laser–matter interactions. It is now well understood that when a laser is tuned near an electric dipole transition, the permittivity of the material can be strongly modified, giving rise to a whole family of optical effects. For example, using EIT and related ideas, light can be slowed down, stopped, or even forced to move backward, and optical nonlinearities can be made large enough to be effective at the single-photon level (Fleischhauer and Lukin, 2000; Gea-Banacloche et al., 1995; Gehring et al., 2006; Hau et al., 1999; Imamoglu et al., 1997; Kang and Zhu, 2003; Kash et al., 1999; Kocharovskaya and Mandel, 1990; Lukin and Imamoglu, 2000; Phillips et al., 2001, 2008; Wang et al., 2001). Up until very recently, these atomic physics experiments have not been truly comparable to metamaterials work since there has been negligible interaction with the magnetic field of light. As we discussed earlier, recent experiments have shown that using magnetic dipole transitions of rare-earth ions in doped crystals, it is possible to interact strongly with the magnetic field of a laser beam and modify permeability of the material significantly. Although it has not yet been possible to achieve a negative refractive index using atomic transitions, recent experiments hold considerable promise for studying negative index physics in the near future.

For the last 2 decades, negative index research has emerged as an exciting field of science and has already made a large impact on a number of scientific

disciplines. In our view, this research is important from both a fundamental and also a practical point of view. On the fundamental side, many of the features of electromagnetic waves in these systems are unique (left-handedness, negative refraction, reverse Doppler effect, etc.), and as a result, they are exciting to study and understand. On the practical side, it appears clear that these materials extend the range and impact of available optical tools. Up until now, negative index materials have only been constructed using artificially engineered structures that have the desired properties over a certain wavelength range. Atomic transitions offer an alternative and in many ways complementary approach to building negative index materials. It is clear that there are both drawbacks and advantages of using atomic transitions instead of the traditional structured metamaterials. One key drawback is that using this method we are limited to transitions provided to us by nature; i.e., the wavelengths that can be used are limited by the magnetic dipole transitions of rare earths. Another drawback is the intrinsically narrow bandwidth of the atomic transitions. However, there are also clear fundamental and practical advantages of atomic transitions. The feature scale of the constructed devices using the atomic approach is determined by the lattice constant of the crystal, which is more than two orders of magnitude smaller compared to typical feature scale of engineered metamaterials. As a result, the atomic approach may produce negative index lenses with far-better imaging resolution. Also, the atomic approach is uniquely suited for combining negative index materials with single-photon storage and emission devices. As a result, if experimentally observed, negative index materials using atomic transitions may form the fundamental building block of future “quantum metamaterials,” with many exciting and important applications.

## ACKNOWLEDGMENTS

We thank Nick Brewer, Zach Simmons, Eli Mueller, and Dan Sikes for their contributions to both the ideas and the experiments that have been presented in this review chapter. This work has been supported by the Air Force Office of Scientific Research (AFOSR), Wisconsin Alumni Research Foundation (WARF), and start-up funds from the University of Wisconsin-Madison. We specifically would like to acknowledge AFOSR program officer Tatjana Curcic, for her support to our negative index project for many years.

## REFERENCES

- Aikawa, K., Frisch, A., Mark, M., Baier, S., Rietzler, A., Grimm, R., Ferlaino, F., 2012. Bose-Einstein condensation of erbium. *Phys. Rev. Lett.* 108, 210401.
- Berglund, A.J., Hanssen, J.L., McClelland, J.J., 2008. Narrow-line magneto-optical cooling and trapping of strongly magnetic atoms. *Phys. Rev. Lett.* 100, 113002.

- Boardman, A.D., Grimalsky, V.V., Kivshar, Y.S., Koshevaya, S.V., Lapine, M., Litchinitser, N.M., Malnev, V.N., Noginov, M., Rapoport, Y.G., Shalaev, V.M., 2011. Active and tunable metamaterials. *Laser Photonics Rev.* 5, 287.
- Brewer, N.R., Buckholtz, Z.N., Simmons, Z.J., Mueller, E.A., Yavuz, D.D., 2017. Coherent magnetic response at optical frequencies using atomic transitions. *Phys. Rev. X* 7, 011005.
- Carnall, W.T., Fields, P.R., Rajnak, K., 1968. Electronic energy levels of the trivalent lanthanide aquo ions:  $Tb^{+3}$ . *J. Chem. Phys.* 49, 4447.
- Chen, H.T., Taylor, A.J., Yu, N., 2016. A review of metasurfaces: physics and applications. *Rep. Prog. Phys.* 79, 076401.
- Cowan, R.D., 1981. *The Theory of Atomic Structure and Spectra*. University of California Press, Berkeley.
- Cubukcu, E., Aydin, K., Ozbay, E., Foteinopoulou, S., Soukoulis, C.M., 2003. Sub-wavelength resolution in a two-dimensional photonic crystal based Superlens. *Phys. Rev. Lett.* 91, 207401.
- Dieke, G.H., Crosswhite, H.M., 1963. The spectra of the doubly and triply ionized rare earths. *Appl. Optics* 2, 675.
- Equall, R.W., Sun, Y., Cone, R.L., Macfarlane, R.M., 1994. Ultraslow optical dephasing in  $Eu^{+3}:Y_2SiO_5$ . *Phys. Rev. Lett.* 72, 2179.
- Ergin, T., Stenger, N., Brenner, P., Pendry, J.B., Wegener, M., 2010. Three-dimensional invisibility cloak at optical wavelengths. *Science* 327, 337.
- Fang, N., Lee, H., Sun, C., Zhang, X., 2005. Sub-diffraction-limited optical imaging with a silver Superlens. *Science* 308, 534.
- Ferraria, L., Wu, C., Lepaged, D., Zhang, X., Liua, Z., 2015. Hyperbolic metamaterials and their applications. *Prog. Quant. Electron.* 40, 1.
- Fleischhauer, M., 1999. Optical pumping in dense atomic media: limitations due to reabsorption of spontaneously emitted photons. *Europhys. Lett.* 45, 659.
- Fleischhauer, M., Lukin, M.D., 2000. Dark state polaritons in electromagnetically induced transparency. *Phys. Rev. Lett.* 84, 5094.
- Fukuhara, T., Sugawa, S., Takahashi, Y., 2007. Bose–Einstein condensation of an ytterbium isotope. *Phys. Rev. A* 76, 051604.
- Gea-Banacloche, J., Li, Y., Jin, S., Xiao, M., 1995. Electromagnetically induced transparency in ladder-type inhomogeneously broadened media: theory and experiment. *Phys. Rev. Lett.* 74, 2447.
- Gehring, G.M., Schweinsberg, A., Barsi, C., Kostinski, N., Boyd, R.W., 2006. Observation of backward pulse propagation through a medium with a negative group velocity. *Science* 312, 895.
- Glybovski, S. B., Tretyakov, S. A., Belov, P. A., Kivshar, Y. S., Simovski, C. R., 2016. Metasurfaces: from microwaves to visible. *Phys. Reports* 634, 1 (2016).
- Ham, B.S., Hemmer, P.R., Shahriar, M.S., 1997. Efficient electromagnetically induced transparency in a rare-earth doped crystal. *Opt. Commun.* 144, 227.
- Ham, B.S., Hemmer, P.R., Shahriar, M.S., 1999. Efficient phase conjugation via two-photon coherence in an optically dense crystal. *Phys. Rev. A* 59, 2583.
- Harris, S.E., 1997. Electromagnetically induced transparency. *Phys. Today* 50 (7), 36.
- Hau, L.V., Harris, S.E., Dutton, Z., Behroozi, C.H., 1999. Light speed reduction to 17 m/s in an ultracold atomic gas. *Nature* 397, 594.
- Hess, O., Pendry, J.B., Maier, S.A., Oulton, R.F., Hamm, J.M., Tsakmakidis, K.L., 2012. Active nanoplasmonic metamaterials. *Nat. Mater.* 11, 573.
- High, A.A., Devlin, R.C., Dibos, A., Polking, M., Wild, D.S., Perczel, J., de Leon, N.P., Lukin, M.D., Park, H., 2015. Visible-frequency hyperbolic metasurface. *Nature* 522, 192.
- Houck, A.H., Brock, J.B., Chuang, I.L., 2003. Experimental observations of a left-handed material that obeys Snells law. *Phys. Rev. Lett.* 90, 137401.

- Imamoglu, A., Schmidt, H., Woods, G., Deutsch, M., 1997. Strongly interacting photons in a nonlinear cavity. *Phys. Rev. Lett.* 79, 1467.
- Jahani, S., Jacob, Z., 2016. All-dielectric metamaterials. *Nat. Nanotechnol.* 11, 23.
- Kang, H., Zhu, Y., 2003. Observation of large Kerr nonlinearity at low light intensities. *Phys. Rev. Lett.* 91, 093601.
- Kash, M. M., Sautenkov, V. A., Zibrov, A. S., Hollberg, L., Welch, G. R., Lukin, M. D., Rostovtsev, Y., Fry, E. S., Scully, M., O., 1999. Ultraslow group velocity and enhanced nonlinear effects in a coherently driven atomic gas. *Phys. Rev. Lett.* 82, 5229.
- Kasperczyk, M., Person, S., Ananias, D., Carlos, L.D., Novotny, L., 2015. Excitation of magnetic dipole transitions at optical frequencies. *Phys. Rev. Lett.* 114, 163903.
- Kastel, J., Fleischhauer, M., Yelin, S.F., Walsworth, R.L., 2007. Tunable negative refraction without absorption via electromagnetically induced chirality. *Phys. Rev. Lett.* 99, 073602.
- Kastel, J., Fleischhauer, M., Yelin, S.F., Walsworth, R.L., 2009. Low-loss negative refraction by laser-induced magnetoelectric cross coupling. *Phys. Rev. A* 79, 063818.
- Klein, J., Beil, F., Halfmann, T., 2007a. Rapid adiabatic passage in a  $\text{Pr}^{+3}:\text{Y}_2\text{SiO}_5$  crystal. *J. Phys. B: At. Mol. Opt. Phys.* 40, 345.
- Klein, J., Beil, F., Halfmann, T., 2007b. Robust population transfer by stimulated Raman adiabatic passage in a  $\text{Pr}^{+3}:\text{Y}_2\text{SiO}_5$  crystal. *Phys. Rev. Lett.* 99, 113003.
- Klein, J., Beil, F., Halfmann, T., 2008. Experimental investigations of stimulated Raman adiabatic passage in a doped solid. *Phys. Rev. A* 78, 033416.
- Kocharovskaya, O., Mandel, P., 1990. Amplification without inversion, the double-lambda scheme. *Phys. Rev. A* 42, 523.
- Kolesov, R., Xia, K., Reuter, R., Stohr, R., Zappe, A., Meijer, J., Hemmer, P.R., Wrachtrup, J., 2012. Optical detection of a single rare-earth ion in a crystal. *Nat. Commun.* 3 (1029), 1.
- Konz, F., Sun, Y., Thiel, C.W., Cone, R.L., Equall, R.W., Hutcheson, R.L., Macfarlane, R.M., 2003. Temperature and concentration dependence of optical dephasing, spectral-hole lifetime, and anisotropic absorption in  $\text{Eu}^{+3}:\text{Y}_2\text{SiO}_5$ . *Phys. Rev. B* 68, 085109.
- Krupke, W.F., 1966. Optical absorption and fluorescence intensities in several rare-earth-doped  $\text{Y}_2\text{O}_3$  and  $\text{LaF}_3$  single crystals. *Phys. Rev.* 145, 325.
- Lapine, M., Shadrivov, I.V., Kivshar, Y.V., 2014. Colloquium: nonlinear metamaterials. *Rev. Mod. Phys.* 86, 1093.
- Lauritzen, B., Hastings-Simon, S.R., de Rietmatten, H., Afzelius, M., Gisin, N., 2008. State preparation by optical pumping in erbium-doped solids using stimulated emission and spin mixing. *Phys. Rev. A* 78, 043402.
- Lauritzen, B., Timoney, N., Gisin, N., Afzelius, M., de Rietmatten, H., Sun, Y., Macfarlane, R.M., Cone, R.L., 2012. Spectroscopic investigations of  $\text{Eu}^{+3}:\text{Y}_2\text{SiO}_5$  for quantum memory applications. *Phys. Rev. B* 85, 115111.
- Lezec, H.J., Dionne, J.A., Atwater, H.A., 2007. Negative refraction at visible frequencies. *Science* 316, 430.
- Liu, G.K., Huang, J., Cone, R.L., Jacquier, B., 1988. Spectral hole burning, Zeeman effect, and hyperfine structure for  $\text{Tb}^{+3}:\text{LiYF}_4$ . *Phys. Rev. B* 38, 11061.
- Lu, M., Youn, S.H., Lev, B.J., 2010. Trapping ultracold dysprosium: a highly magnetic gas for dipolar physics. *Phys. Rev. Lett.* 104, 063001.
- Lu, M., Burdick, N.Q., Lev, B.L., 2012. Quantum degenerate dipolar Fermi gas. *Phys. Rev. Lett.* 108, 215301.
- Lukin, M.D., Imamoglu, A., 2000. Nonlinear optics and quantum entanglement of ultraslow photons. *Phys. Rev. Lett.* 84, 1419.
- Macfarlane, R.M., 2002. High-resolution laser spectroscopy of rare-earth doped insulators: a personal perspective. *J. Lumin.* 100, 1.

- Macfarlane, R.M., Shelby, R.M., 1987. Homogeneous line broadening of optical transitions of ions and molecules in glasses. *J. Lumin.* 36, 179.
- McAuslan, D.L., Bartholomew, J.G., Sellars, M.J., Longdell, J.J., 2012. Reducing decoherence in optical and spin transitions in rare-earth-metal-ion-doped materials. *Phys. Rev. A* 85, 032339.
- McClelland, J.J., Hanssen, J.L., 2006. Laser cooling without repumping: a magneto-optical trap for erbium atoms. *Phys. Rev. Lett.* 96, 143003.
- Moitra, P., Yang, Y., Anderson, Z., Kravchenko, I.I., Briggs, D.P., Valentine, J., 2013. Realization of an all-dielectric zero-index optical metamaterial. *Nat. Photon.* 7, 791.
- Ofelt, G.S., 1962. Structure of the  $f^6$  configuration with application to rare-earth ions. *J. Chem. Phys.* 38, 2171.
- Oktel, M.O., Mustecaplioglu, O.E., 2004. Electromagnetically induced left-handedness in a dense gas of three-level atoms. *Phys. Rev. A* 70, 053806.
- Oliviera, S.L., Rand, S.C., 2007. Intense nonlinear magnetic dipole radiation at optical frequencies: molecular scattering in a dielectric liquid. *Phys. Rev. Lett.* 98, 093901.
- Orth, P.P., Hennig, R., Keitel, C.H., Evers, J., 2013. Negative refraction with tunable absorption in an active dense gas of atoms. *N. J. Phys.* 15, 013027.
- Peijzel, P.S., Meijerink, A., Wegh, R.T., Reid, M.F., Burdick, G.W., 2005. A complete 4f energy level diagram for all trivalent lanthanide ions. *J. Solid State Chem.* 178, 448.
- Pelletier-Allard, N., Pelletier, R., 1985. Magnetic dipole and electric-quadrupole effects in  $Tb^{+3}:LaCl_3$ . *Phys. Rev. B* 31, 2661.
- Pendry, J.B., 2000. Negative refraction makes a perfect lens. *Phys. Rev. Lett.* 85, 3966.
- Pendry, J.B., Aubry, A., Smith, D.R., Maier, S.A., 2012. Transformation optics and sub-wavelength control of light. *Science* 337, 549.
- Phillips, D.F., Fleischhauer, A., Mair, A., Walsworth, R.L., Lukin, M.D., 2001. Storage of light in atomic vapor. *Phys. Rev. Lett.* 86, 783.
- Phillips, N.B., Gorshkov, A.V., Novikova, I., 2008. Optimal light storage in atomic vapor. *Phys. Rev. A* 78, 023801.
- Rand, S.C., Fisher, W.M., Oliveira, S.L., 2008. Optically induced magnetization in homogeneous, undoped dielectric media. *J. Opt. Soc. Am. B* 25, 1106.
- Schurig, D., Mock, J.J., Justice, B.J., Cummer, S.A., Pendry, J.B., Starr, A.F., Smith, D.R., 2006. Metamaterial electromagnetic cloak at microwave frequencies. *Science* 314, 977.
- Scully, M.O., Zubairy, M.S., 1997. *Quantum Optics*. Cambridge University Press, Cambridge.
- Shelby, R.A., Smith, D.R., Shultz, S., 2001. Experimental verification of a negative index of refraction. *Science* 292, 77.
- Shen, X.A., Kachru, R., 1994.  $^7F_0 \rightarrow ^5D_1$  transition in Eu:YSO. *J. Opt. Soc. Am. B* 11, 591.
- Sikes, D.E., Yavuz, D.D., 2010. Negative refraction with low absorption using Raman transitions with magneto-electric coupling. *Phys. Rev. A* 82, 011806.
- Sikes, D.E., Yavuz, D.D., 2011. Negative refraction using Raman transitions and chirality. *Phys. Rev. A* 84, 053836.
- Smith, D.R., Kroll, N., 2000. Negative refractive index in left-handed materials. *Phys. Rev. Lett.* 85, 2933.
- Smolyaninov, I.I., Hung, Y., Davis, C.C., 2007. Magnifying Superlens in the visible frequency range. *Science* 315, 1699.
- Takasu, Y., Honda, K., Komori, K., Kuwamoto, T., Kumakura, M., Takahashi, Y., Yabuzaki, T., 2003. High-density trapping of cold ytterbium atoms by an optical dipole force. *Phys. Rev. Lett.* 90, 023003.
- Taylor, K.N.R., Darby, M.I., 1972. *Physics of Rare Earth Solids*. Chapman and Hall.
- Thomas, K.S., Singh, S., Dieke, G.H., 1963. Energy levels of  $Tb + 3$  in  $LaCl_3$  and other chlorides. *J. Chem. Phys.* 38, 2180.

- Thommen, Q., Mandel, P., 2006. Electromagnetically induced left handedness in optically excited four-level atomic media. *Phys. Rev. Lett.* 96, 053601.
- Turukhin, A.V., Sudarshanam, V.S., Shahriar, M.S., Musser, J.A., Ham, B.S., Hemmer, P.R., 2001. Observation of ultraslow and stored light pulses in a solid. *Phys. Rev. Lett.* 88, 023602.
- Valentine, J., Li, J., Zentgraf, T., Bartal, G., Zhang, X., 2009. An optical cloakmade of dielectrics. *Nat. Mater.* 8, 568.
- Van Pieteron, L., Reid, M.F., Burdick, G.W., Meijerink, A., 2002a.  $4f \rightarrow 4f5d$  transitions of the heavy lanthanides: experiment and theory. *Phys. Rev. B* 65, 045114.
- Van Pieteron, L., Reid, M.F., Wegh, R.T., Soverna, S., Meijerink, A., 2002b.  $4f \rightarrow 4f5d$  transitions of the light lanthanides: experiment and theory. *Phys. Rev. B* 65, 045113.
- Veselago, V.G., 1968. The electrodynamics of substances with simultaneously negative values of  $\epsilon$  and  $\mu$ . *Sov. Phys. Usp.* 10, 509.
- Wang, H., Goorskey, D., Xiao, M., 2001. Enhanced Kerr nonlinearity via atomic coherence in a three-level atomic system. *Phys. Rev. Lett.* 87, 073601.
- Weber, M.J., Schaufele, R.F., 1965. Radiative and nonradiative transitions in the fluorescence decay of  $\text{Eu}^{+3}$  in  $\text{SrTiO}_3$ . *J. Chem. Phys.* 43, 1702.
- Wegh, R.T., Meijerink, A., 1999. Spin-allowed and spin-forbidden  $4f \rightarrow 4f5d$  transitions for heavy lanthanides in fluoride hosts. *Phys. Rev. B* 60, 10820.
- Wybourne, B.G., 1965. *Spectroscopic Properties of Rare-Earths*. John Wiley & Sons.
- Wybourne, B.G., Smentek, L., 2007. *Optical Spectroscopy of Lanthanides*. Taylor & Francis.
- Xianzhong, C., Yu, L., Jingjing, Z., Jiang, K., Pendry, J.B., Shuang, Z., 2011. Macroscopic invisibility cloaking of visible light. *Nat. Commun.* 2, 176.
- Xiao, S., Drachev, V.P., Kildishev, A.V., Xingjie, N., Chettiar, U.K., Hsiao-Kuan, Y., Shalaev, V.M., 2010. Loss-free and active optical negative-index metamaterials. *Nature* 466, 735.
- Yavuz, D.D., 2005. Refractive index enhancement in a far-off resonant atomic system. *Phys. Rev. Lett.* 95, 223601.
- Yavuz, D.D., Brewer, N.R., 2014. Left-handed electromagnetic waves in materials with induced polarization and magnetization. *Phys. Rev. A* 90, 063807.
- Yavuz, D.D., Brewer, N.R., Miles, J.A., Simmons, Z.J., 2013. Suppression of inhomogeneous broadening using the AC stark shift. *Phys. Rev. A* 88, 063836.
- Zhao, Q., Zhou, J., Zhang, F., Lippens, D., 2009. Mie resonance-based dielectric metamaterials. *Mater. Today* 12, 60.

## FURTHER READING

- Foteinopoulou, S., Economou, E.N., Soukoulis, C.M., 2003. Refraction in media with a negative refractive index. *Phys. Rev. Lett.* 90, 107402.
- Harris, S.E., Hau, L.V., 1999. Nonlinear optics at low light levels. *Phys. Rev. Lett.* 82, 4611.
- O'Brien, C., Anisimov, P.M., Rostovtsev, Y., Kocharovskaya, O., 2011. Coherent control of refractive index in far-detuned lambda systems. *Phys. Rev. A* 84, 063835.
- Proite, N.A., Unks, B.E., Green, J.T., Yavuz, D.D., 2008. Refractive index enhancement with vanishing absorption in an atomic vapor. *Phys. Rev. Lett.* 101, 147401.